Atmospheric Environment 313 (2023) 120075

Contents lists available at ScienceDirect

Atmospheric Environment

journal homepage: www.elsevier.com/locate/atmosenv

# Top-down constraints on $N_2O$ emissions from Canada

Cynthia Nevison [a,*], Xin Lan [b,c], Doug Worthy [d], Hanqin Tian [e]

[a] University of Colorado/INSTAAR, Campus Box 0450, Boulder, CO, 80309-0450, USA
[b] NOAA ESRL Global Monitoring Laboratory, Boulder, CO, USA
[c] University of Colorado, Cooperative Institute for Research in Environmental Sciences (CIRES), Boulder, CO, USA
[d] Environment Canada Climate Change, Ontario, Canada
[e] Boston College, Boston, MA, USA

## HIGHLIGHTS

- Canadian cropland emits 0.08 ± 0.08 Tg $N_2O$–N/yr according to a regional inversion.
- This represents ~1% of the global anthropogenic $N_2O$ source.
- Including 4 new Canadian monitoring sites modestly improves inversion uncertainty.
- Canadian cropland $N_2O$ fluxes have comparable freeze-thaw and growing season peaks.

## ARTICLE INFO

*Keywords:*
Nitrous oxide
$N_2O$
Atmospheric inversion
Canada
Agricultural emissions

## ABSTRACT

Canadian nitrous oxide ($N_2O$) emissions over 2011–2015 are estimated using the CarbonTracker-Lagrange (CT-L) regional inversion. The uncertainty in the whole-country total is high, on the order of 100% or more, with a net flux not significantly different from zero. Emissions are better resolved in Canadian cropland, primarily in Alberta, Saskatchewan, and Manitoba, where the total flux is estimated at 0.08 ± 0.08 Tg N/yr. The uncertainty is improved by the addition of 4 new Canadian sites to the inversion, but remains large, mainly due to the low signal to background ratio at all Canadian $N_2O$ measurement sites. The seasonal patterns in Canadian cropland emissions suggest a dual maximum, with a late winter freeze-thaw pulse and a growing season flux of similar magnitude. Overall, Canadian cropland accounts for ~1% of the global anthropogenic $N_2O$ source according to the inversion, although some process-based models suggest a source more on the order of 2%.

## 1. Introduction

Nitrous oxide ($N_2O$) is a long-lived greenhouse gas that has increased from 275 ppb preindustrially to over 336 ppb in 2022, contributing about 6% of the total enhanced anthropogenic greenhouse gas radiative forcing [MacFarling-Meure et al., 2006; Stocker et al., 2013; Lan et al., 2022a]. The photochemical destruction of $N_2O$ in the stratosphere yields $NO_x$, a catalyst of stratospheric ozone depletion [Ravishankara et al., 2009; Prather et al., 2023]. $N_2O$ is produced in soils, freshwater, and oceans, in association with microbial nitrogen cycling, although emissions from individual sources are still highly uncertain [Canadell et al., 2021]. Enhanced microbial N cycling following the application of synthetic nitrogen (N) fertilizer to cropland is thought to be responsible for most of the observed increase in atmospheric $N_2O$ [Crutzen et al., 2008; Park et al., 2012]. However, the partitioning between emissions directly from agricultural fields vs. downstream, e.g., in drainage water, streams or estuaries, is not well known [Beaulieu et al., 2011; Wells et al., 2018].

Atmospheric inversions are a "top-down" method for quantifying $N_2O$ emissions that can be run on a global or regional scale [Miller et al., 2012; Saikawa et al., 2014; Thompson et al., 2014; Wells et al., 2015; Nevison et al., 2018]. Inversions provide a check on "bottom-up" emission estimates, which are based on extrapolations of generally sparse surface flux measurements and/or uncertain process-based models [Xu et al., 2021]. Deng et al. [2022] found that inversions tend to predict higher emissions of $N_2O$ than bottom-up national greenhouse gas inventory methods in tropical countries.

In general, previous $N_2O$ inversions have not explicitly distinguished Canadian $N_2O$ emissions from the broader source region of the North

* Corresponding author.
*E-mail address:* Cynthia.Nevison@colorado.edu (C. Nevison).

https://doi.org/10.1016/j.atmosenv.2023.120075
Received 31 May 2023; Received in revised form 31 August 2023; Accepted 5 September 2023
Available online 7 September 2023

American continent [Saikawa et al., 2014; Nevison et al., 2018; Xu et al., 2021]. However, Canada is one of the largest countries in the world in terms of land area and is an important player in the budget of other greenhouse gases, e.g. for the $CO_2$ land sink [Deng et al., 2022]. Moreover, Canada has set a national goal of reducing on-farm nitrous oxide emissions from synthetic N fertilizer by 30% by 2030 [Gamble and Heaney, 2022], which suggests the value of exploring a potential role for atmospheric inversions in tracking progress toward meeting this target.

In this paper we quantify $N_2O$ emissions from Canada and their uncertainty using the top-down CarbonTracker-Lagrange regional inversion, which is based on National Oceanic and Atmospheric Administration (NOAA) data. We test the sensitivity of the inversion results to the inclusion of 4 additional monitoring sites from Canada as well as to the use of two alternate atmospheric transport models. We examine emissions from the whole country and specifically from Canadian croplands. Finally, we characterize and compare the seasonality of Canadian cropland emissions to those from the U.S. Midwest.

## 2. Methods

### 2.1. Inversion methodology

The model used in this study is the CarbonTracker-Lagrange (CT-L) regional inversion. CT-L is a Bayesian inversion that begins with an objective "cost function" **J(s)**,

$$\mathbf{J}(\mathbf{s}) = \frac{1}{2}(z - Hs)^{\mathrm{T}}\mathbf{R}^{-1}(\mathbf{z} - \mathbf{Hs}) + \frac{1}{2}(\mathbf{s} - \mathbf{s_p})^{\mathrm{T}}\mathbf{Q}^{-1}(\mathbf{s} - \mathbf{s_p}), \quad (1)$$

The cost function is minimized and solved for optimized fluxes using algorithms described by *Yadav and Michalak* [2013].

$$\hat{\mathbf{s}} = \mathbf{s_p} + (\mathbf{HQ})^{\mathrm{T}} * (\mathbf{HQH^T} + \mathbf{R})^{-1} * (\mathbf{z\text{-}Hs_p}) \quad (2)$$

where,

$\mathbf{s}_{(m\ x\ 1)}$ is the surface flux in nmol $m^{-2}$ $s^{-1}$.
$\hat{\mathbf{s}}_{(m\ x\ 1)}$ is the optimized surface flux in nmol $m^{-2}$ $s^{-1}$.
$\mathbf{s_p}$ $_{(m\ x\ 1)}$ is the prior estimate of **s.**
$\mathbf{z}_{(n\ x\ 1)}$ is a vector of $N_2O$ observations, corrected by subtracting an empirical background value, in ppb.
$\mathbf{H}_{(n\ x\ m)}$ is a transport matrix, in ppb/(nmol $m^{-2}$ $s^{-1}$) that describes the relationship between the surface fluxes **s** and the observations **z.**
$\mathbf{R}_{(n\ x\ n)}$ is the model-data mismatch error covariance matrix, in $ppb^2$.
$\mathbf{Q}_{(m\ x\ m)}$ is the prior flux covariance error matrix, in (nmol $m^{-2}$ $s^{-1}$)$^2$ which is computed from a prescribed prior flux error vector $\sigma_s$ in nmol $m^{-2}$ $s^{-1}$, temporal correlation length in days and spatial correlation length in km.

The dimensions of the equation are defined as follows,
*m* is the number of surface fluxes solved for in both time and space.
*n* is the number of atmospheric observations.

The model configuration used here is similar to that described in detail in Nevison et al. [2018]. The prior was adapted from the year 2000 posterior flux of the global atmospheric $N_2O$ inversion of Saikawa et al. [2014] (Fig. S1). Spatial and temporal correlation lengths of 300 km and 35 days, respectively, were used in **Q**. Two alternative sets of parameters for $\sigma_s$ and **R** were used to represent alternative scenarios of more constrained prior/relaxed model-data mismatch (Case 1) and more relaxed prior/constrained model-data mismatch (Case 2) (see Table S1 for details). The square root $\sigma_r$ of the main diagonal components of **R** was 0.84 and 0.75 for Case 1 and 2, respectively.

The **H** matrices in Nevison et al. [2018] were constructed from 10-day back trajectory surface influence footprints from a single particle dispersion model, the Stochastic Time-Inverted Lagrangian Transport (STILT) model [Lin et al., 2003], where STILT was driven by a Weather Research and Forecasting model (WRF) simulation customized for Lagrangian modeling [Nehrkorn et al., 2010]. The current study uses both WRF-STILT and, alternatively, the Hybrid Single-Particle Lagrangian Integrated Trajectory (HYSPLIT) [Draxler and Hess, 1998; Stein et al., 2015], which is driven by the North American Mesoscale Forecast System (NAM) model. NAM has ~12 km resolution and is the primary operational model used for mesoscale forecasting by the National Weather Service (NWS). The NAMS meteorological fields provided by the NOAA Air Resources Laboratory are archived in collaboration with the NWS, where the "S" in NAMS signifies that the meteorological fields are archived on the native "sigma" vertical levels of the model.

The atmospheric $N_2O$ data used in CT-L are primarily from the NOAA Global Greenhouse Gas Reference Network (GGGRN) (https://gml.noaa.gov/ccgg/about.html). For the current study, additional flask-air and *in situ* data from Environment and Climate Change Canada (ECCC) were incorporated to expand the network coverage to central and eastern Canada (Fig. 1). CT-L does not require an initial condition. Rather, each atmospheric $N_2O$ observation is adjusted by subtracting an empirically determined background value to compute the vector **z**. The background values are estimated based on the intersection, at the time and location that they leave the CT-L North American domain, of the 10-day back trajectories (which are used as described above to compute the surface influence footprints in **H)** with a 4-dimensional time-varying field covering North America and its surrounding oceans [Nevison et al., 2018].

The NOAA GGRN includes ~ weekly paired flask samples from ground-based sites [Lan et al., 2022], as well as tall towers [Andrews et al., 2014, 2022] and small aircraft [Sweeney et al., 2015; McKain et al., 2022] that use programmable 12-flask sampling systems. All samples are shipped to the NOAA Global Monitoring Laboratory in Boulder, Colorado, USA for analysis of $N_2O$ on a gas chromatograph with electron capture detection (ECD), calibrated with a suite of standards on the WMO X2006A scale maintained by NOAA GML (Hall et al., 2007). Uncertainties of the measurements (68% confidence interval) for the period of this study range from 0.26 to 0.43 ppb. The data were filtered to exclude air samples collected 4000 m or more above the local surface. These data generally had small surface influence footprints but were influenced occasionally by episodic stratospheric intrusions of highly $N_2O$-depleted air, which the inversion framework is not well equipped to handle.

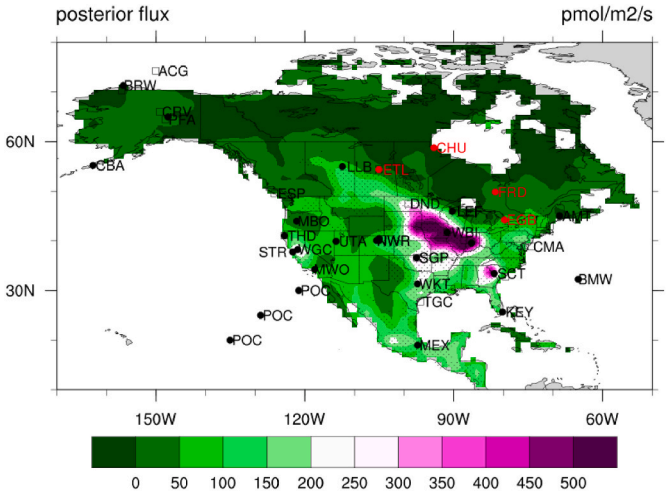


**Fig. 1.** Mean posterior $N_2O$ emissions for 2011–2015 for Cases 1 and 2 using NOAA $N_2O$ data only and STILT-WRF footprints [Lin et al., 2003; Nehrkorn et al., 2010]. Stippling shows areas in which more than 10% of the land is planted in crops. $N_2O$ observation sites from NOAA GGGRN (circles = surface-based, magenta squares = aircraft) are superimposed. Selected stations are labeled where permitted by legibility. The locations of the 4 additional ECCC sites are shown in red.

Over the past two decades, ECCC has built an observational network for greenhouse gases that currently stands at 25 continuous ground-based stations in Canada. Some of these sites are augmented with weekly flask sampling. The network has focused primarily on $CO_2$ and $CH_4$ and has recently phased out most $N_2O$ measurements, but high quality $N_2O$ data are available for about a decade, from 2007 to late 2015/early 2016 at 4 ECCC sites, as summarized in Table 1. For the CT-L inversion, the ECCC flask-air measurements were merged with *in situ* data at EGB, FRD, and ETL to fill various gaps in the continuous data. The *in situ* data were measured continuously, but were provided as daily averages, using afternoon data only, to match the 2 p.m. time stamp of the WRF-STILT surface influence footprints. If both *in situ* and flask data were available on the same day, *in situ* data were used preferentially. The ECCC data were measured by gas chromatography with electron capture detection (ECD) on the same scale as NOAA. Intercomparisons of weekly flask air samples at Alert (1999–2016) between ECCC and NOAA show that the mean offset between NOAA and ECCC is less than 0.05 ppb but with variations in offsets from one year to the next in the range of ±0.3 ppb. ECCC flask and *in situ* data intercomparisons at FRD and ETL over a 10+ year period show a similar mean offset near zero and also a range of ±0.3 ppb from one year to the next.

For the current study, the CT-L inversion was run with a daily time step for each year from January 1, 2011 to December 31, 2015, the time frame when ECCC coverage was densest. For computational reasons, this 5-year time span was divided into 5 separate, partly overlapping inversions. These were centered around each calendar year but padded by the previous December and the following January to avoid end effects that could occur if Equation 2 in the inversion were solved without information about fluxes preceding or following the start or finish of the year, respectively. The combined NOAA + ECCC simulations were run only with WRF-STILT **H** matrices, since only WRF-STILT footprints were available for the ECCC sites, while the NOAA-only simulations were run for both WRF-STILT and NAMS-HYSPLIT.

### 2.2. Countrywide and regional integrals

The analysis of the posterior inversion fluxes included integrating daily $N_2O$ fluxes over 1) Canada as a whole and 2) Canadian Cropland. These regions were delineated based on a gridded database that distinguished national boundaries. A further filter was applied to identify Canadian Cropland using an agricultural dataset with units of percentage of total grid area planted in major crop types, based on the 10 km resolution dataset of *Ramankutty and Foley* [1998], which was regridded to 0.5° × 0.5° degree by *Levis et al.* [2012]. Canadian Cropland was defined as the region in which at least 10% of land was covered in crops of any kind. This region mainly encompasses the agricultural belt in Alberta, Saskatchewan, and Manitoba, with extensive plantings of crops such as wheat, canola, and barley, but also includes agricultural land in southern Ontario and Quebec. The entire $N_2O$ flux within each agricultural grid cell was included in the Canadian Cropland integral.

For each integrated region, a regionally aggregated posterior flux covariance matrix was computed to estimate the uncertainty in the aggregated fluxes. The posterior flux covariance matrix was computed monthly as a function of **Q**, **H** and **R** [e.g., Yadav and Michalak, 2013] and was extrapolated daily by linearly interpolating between months. In addition to individual annual seasonal cycles, the multi-year mean seasonal cycle over 2011–2015 (N = 5 years) was computed and the corresponding mean posterior flux uncertainty was estimated as the inverse square root of 1/N times the sum of the inverse square root of the uncertainties for each year. This mean uncertainty was designed to represent the typical uncertainty in any given year with the assumption that there was no reduction in uncertainty achieved by averaging over the 5-year span.

**Table 1**
Environment and Climate Change Canada (ECCC) $N_2O$ measurement sites used in the inversion.

| Site | Latitude (°N) | Longitude (°W) | In Situ Dates | N | Flask Dates | N |
|---|---|---|---|---|---|---|
| Egbert (EGB) | 44.23°N | 79.78°W | 1/07–8/19 | 4198 | 3/05 - 2/16 | 173 |
| Fraserdale (FRD) | 49.87°N | 81.57°W | 1/07 - 7/14 | 2117 | 1/07 - 2/16 | 654 |
| East Trout Lake (ETL) | 54.35° | 104.99°W | 1/07 - 2/15 | 2540 | 10/05–12/15 | 549 |
| Churchill (CHU)[a] | 58.74°N | 93.82°W | NA | 0 | 4/07–12/15 | 616 |

[a] Flask only. All other sites maintained continuous *in situ* sampling augmented with weekly flask sampling.

## 3. Results

The NOAA-only inversion finds that the major hotspot of $N_2O$ emissions from North America occurs in the U.S. Midwest corn and soybean belt, which receives heavy input of synthetic N fertilizer (Fig. 1). The spatial pattern of the emissions is similar for both Case 1 and Case 2 parameters (Fig. S1). Although much smaller than in the U.S. Midwest, the largest emissions from Canada are also in agricultural regions, particularly the belt extending from the southwest corner of Manitoba through southern Saskatchewan and into Alberta. Much of the remainder of Canada, as well as Alaska, has near zero or even negative fluxes (see discussion below). The four newly added ECCC sites form a ring around a negative flux region centered in northern Ontario (Fig. 1).

The addition of the ECCC data creates modest changes in the posterior $N_2O$ flux over North America (Fig. 2). The largest change is an enhancement in the flux in southern Ontario near the EGB site (Fig. 2c). In contrast, the fluxes decrease slightly near FRD in northern Ontario. The (flask-only) CHU site in Manitoba has little impact either way, i.e., the fluxes are similar with or without the ECCC data. Small enhancements in the fluxes near ETL are discernible, although these occur mainly to the north of cropland in Saskatchewan. Overall, inclusion of the ECCC sites leads to a 0.01 to 0.02 TgN/yr increase in emissions from Canadian Cropland, representing a ~10–25% increase in the total flux relative to the NOAA-only configuration, which is not significant within the range of uncertainty (Table 2). The ECCC sites lead to a small (~1%) decrease in the U.S. flux (Table 2). The impact of the sites on total U.S. + Canada $N_2O$ emissions is similarly very small, since U.S. fluxes dominate Canadian fluxes by more than a factor of 10.

The addition of ECCC data also modestly improves the flux uncertainty reduction achieved by the inversion, most notably in the vicinity of the ECCC sites and by 3–9% over much of central Canada (Fig. 2d). The absolute uncertainty reduction is brought up to about 35% in south central Canada but is still only about 15% at best over the rest of Canada (Fig. 2b). In comparison, in the U.S. Midwest, the best resolved region of the inversion, the uncertainty reduction is on the order of 50%.

The daily integrated $N_2O$ fluxes over Canadian Cropland are characterized by a large regionally aggregated uncertainty, especially for the Case 2 parameters (Fig. 3). The inclusion of ECCC data increases the flux in most times of the year, particularly in summer, and improves the uncertainty reduction throughout the year (Fig. 3a). The STILT and HYSPLIT transport models yield generally comparable results, with a tendency toward larger uncertainty with HYSPLIT (Fig. 3c). Similar patterns occur when comparing STILT and HYSPLIT for the Case 1 configuration, except that the uncertainty envelope is smaller for both transport models compared to Case 2 and is less prone to encompassing negative fluxes (Supplementary Fig. S2).

When averaged over 2011–2015, a dual maximum seasonal cycle is discernible in the posterior fluxes in Canadian Cropland, with peaks of similar magnitude centered around the end of March and the middle of June. The inclusion of ECCC data tends to preferentially enhance the

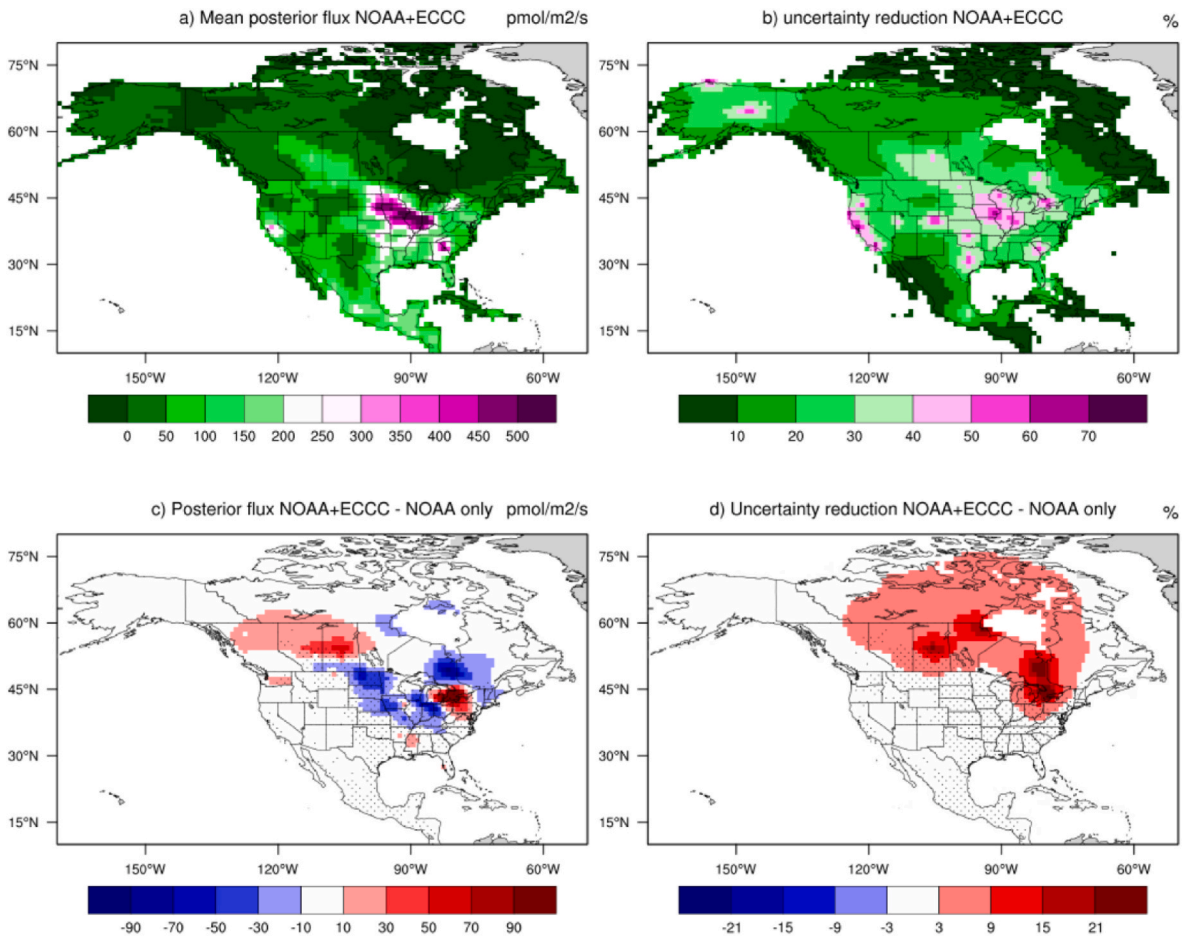


**Fig. 2.** a) Same as contour plot in Fig. 1 except shows mean posterior $N_2O$ emissions using NOAA data plus the 4 ECCC sites. b) Reduction in posterior $N_2O$ flux uncertainty relative to the prior using NOAA plus ECCC data. c) Difference in mean posterior $N_2O$ emissions using NOAA plus ECCC data minus NOAA only data. d) Difference in the reduction in posterior flux uncertainty relative to the prior for NOAA plus ECCC minus NOAA only. All results reflect the 2011–2015 mean. Stippling shows areas in which more than 10% of the land is planted in crops.

**Table 2**
Mean annual $N_2O$ flux for different configurations of the CT-L inversion.

| Transport Model | CT-L Case | ECCC data included | Canada Cropland TgN/yr | Canada TgN/yr | USA TgN/yr |
|---|---|---|---|---|---|
| STILT | 1 | No | 0.08 ± 0.06 | 0.13 ± 0.16 | 1.02 ± 0.13 |
| STILT | 1 | Yes | 0.09 ± 0.05 | 0.15 ± 0.13 | 1.01 ± 0.12 |
| HYSPLIT | 1 | No | 0.08 ± 0.07 | 0.09 ± 0.18 | 1.10 ± 0.15 |
| STILT | 2 | No | 0.07 ± 0.11 | 0.08 ± 0.26 | 1.00 ± 0.21 |
| STILT | 2 | Yes | 0.09 ± 0.08 | 0.12 ± 0.21 | 0.99 ± 0.18 |
| HYSPLIT | 2 | No | 0.08 ± 0.13 | 0.02 ± 0.30 | 1.08 ± 0.24 |

June peak (Fig. 3, Supplementary Fig. S2). In all configurations, the 5-year mean seasonal cycle smooths over the substantial interannual variability in individual years, with some years showing no clear seasonal pattern (Supplementary Fig. S3).

The integrated whole Canada 2011–2015 mean time series has a maximum typically in March and a tendency toward negative values in late summer, particularly in July and particularly for Case 2 and for HYSPLIT (Supplementary Fig. S4). The annual mean total flux ranges from 0.02 to 0.15 Tg N/yr. The annual mean uncertainty is comparable in magnitude to the mean flux in both STILT Case 1 configurations (i.e., 100% uncertainty) and generally substantially exceeds the mean flux (i.e., 200% uncertainty or more) in all Case 2 and HYSPLIT configurations.

## 4. Discussion

### 4.1. Countrywide totals

The CT-L posterior $N_2O$ fluxes in Canada have a large variability across configurations, and a large uncertainty that eclipses the annual mean in 7 out of 8 model configurations (Table 2). Even in the remaining configuration, which uses NOAA and ECCC $N_2O$ data with Case 1 parameters and STILT footprints, the uncertainty is nearly 100% of the mean (0.15 ± 0.13 TgN/yr). Collectively, these results suggest that Canada as a whole is not well resolved by the regional inversion.

Global inversions also have given widely varying estimates of the total $N_2O$ flux from Canada, although Canadian fluxes per se generally are not distinguished from the broader continent of North America. In an analysis of output from a recent model intercomparison, the annual mean Canadian flux ranged from 0.057 to 0.175 TgN/yr, with wide areas of negative fluxes in 3 out 5 global inversions [Thompson et al., 2014, 2019; Wilson et al., 2014; Wells et al., 2015; Patra et al., 2018; Xu et al., 2021]. The mean total Canadian flux was 0.12 ± 0.044 Tg N/yr, in good agreement with CT-L within the (large) margin of uncertainty. The global inversions included 3 Canadian sites, all of which are part of the NOAA GGGRN: Alert (82.45°N, −62.52°W), Estevan Point, British Columbia (49.4°N, −126.55°W), and Lake La Biche, Alberta (54.95°N,

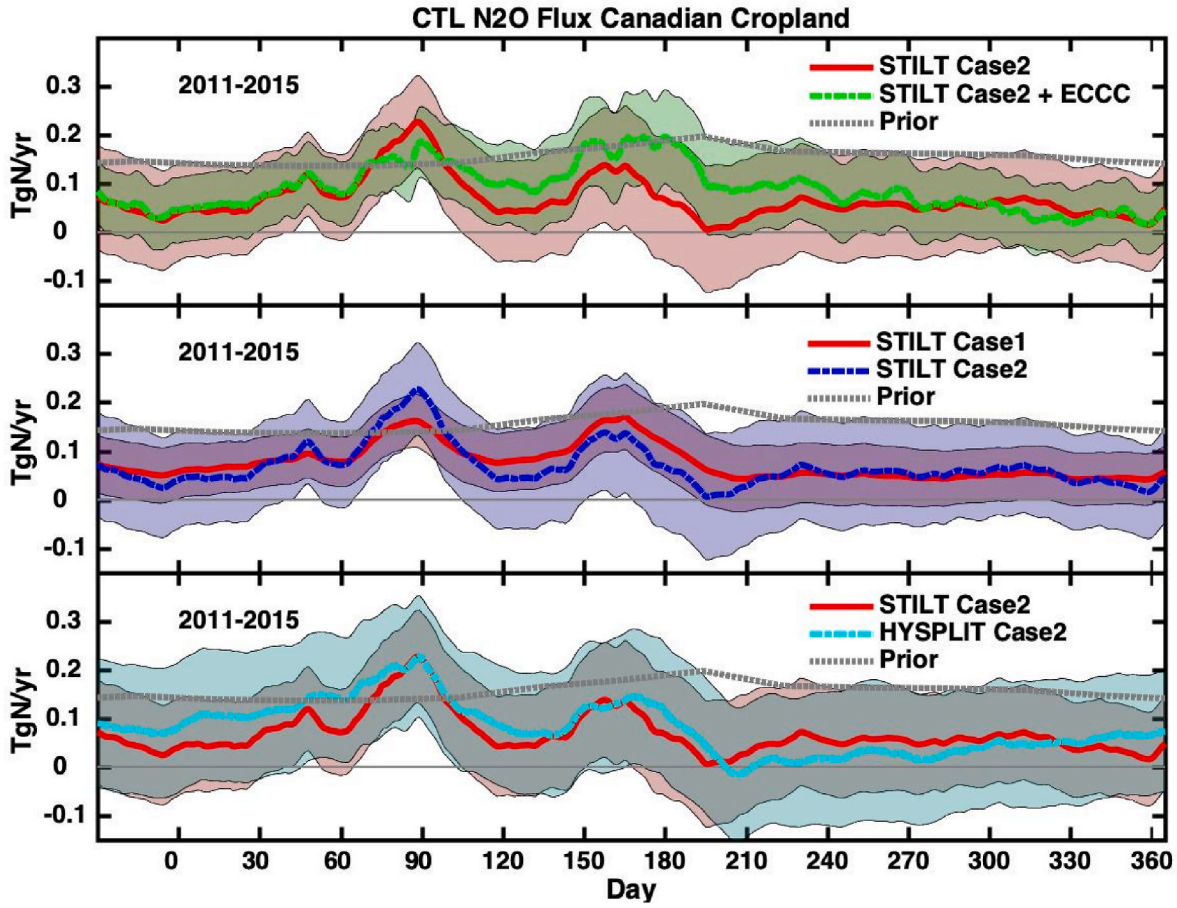


**Fig. 3.** Posterior $N_2O$ flux integrated over Canadian Cropland. The three panels compare the 2011–2015 mean: a) using the STILT particle dispersion model and Case 2 parameters (more relaxed prior/constrained model-data mismatch) for NOAA only $N_2O$ (red) vs. NOAA + ECCC (green), b) Case 1 (red) and Case 2 (blue) using NOAA only and STILT, c) Case 2 using NOAA only and STILT (red) vs HYSPLIT (cyan). The prior flux is shown as a gray dotted line.

−112.45°W), as well as 2 sites in Alaska.

### 4.2. Negative fluxes

Negative $N_2O$ fluxes from Canada are common in both CT-L and global inversion results. While soil uptake of $N_2O$ has been observed in some field studies, particularly in arid regions [Schlesinger, 2013], it is believed to be a relatively small term in the global budget [Ciais et al., 2013]. Therefore, the negative $N_2O$ fluxes predicted by regional and global inversions are probably not biogeochemically realistic.

Negative fluxes are a particularly prominent feature of the CT-L HYSPLIT runs (Fig. 3, Supplementary Figs. S2 and S4). This result can be traced in part to the HYSPLIT background value, which typically is 0.05 ppb on average higher than the corresponding STILT background value. Since CT-L is based upon equations that use observed atmospheric $N_2O$ minus a prescribed background value and since many Canadian data are close to background, a small adjustment of 0.05 ppb can mean the difference between net negative and net positive fluxes.

However, even the STILT CT-L configurations predict negative fluxes in much of Northern Canada, especially in July and August. The latter are months of the seasonal minimum in $N_2O$ at remote sites, likely due to the influence of transport of depleted air from the stratosphere [Liang et al., 2008; Nevison et al., 2018]. They are also months in which $N_2O$ fluxes drop substantially, even in the well-resolved Midwestern U.S. corn and soybean belt, possibly because the spring N fertilizer application has either been sequestered in the growing crop by late summer or already mainly lost from soil due to leaching and denitrification [Nevison et al., 2018]. Given the current uncertainties, a parsimonious interpretation of the inversion results is that $N_2O$ fluxes are not significantly different from zero from Canadian Cropland in late summer and from much of the rest of Canada year round.

### 4.3. Canadian Cropland

Canadian Cropland is better resolved by CT-L than Canada as a whole, with uncertainty as low as ± 55% of the annual mean. The average annual mean flux across different CT-L configurations is 0.08 ± 0.08 Tg N/yr from Canadian Cropland, in good agreement with the national GHG inventory method (~0.08 Tg N/yr) [Xu et al., 2021]. However, process-based models predict agricultural emissions from Canada that are twice as high (~0.15 ± 0.15 Tg N/yr) as those from the national GHG inventory method [Xu et al., 2021]. The large uncertainty of the CT-L estimate suggests that the inversion is currently of limited utility in tracking progress toward Canada's 30% $N_2O$ emissions reduction target in fertilized cropland.

Compared to the prior flux, the posterior flux from CT-L, integrated over Canadian Cropland, is generally lower in all months, except for the March and June peaks (Fig. 3). The prior for this study was based on global inversion results, which in turn used EDGAR-based prior $N_2O$ fluxes that assumed a globally uniform emission coefficient of $N_2O$ from N fertilizer (EDGAR, 2009). In contrast, CT-L results tend to suggest that northern agricultural systems may have lower $N_2O$ emission coefficients per unit fertilizer input compared to temperate systems [Nevison et al., 2018], which may explain the discrepancy between the prior and posterior fluxes in Fig. 3.

When the CT-L result for Canadian Cropland is divided by the total

anthropogenic $N_2O$ source of 7.3 Tg N/yr [Tian et al., 2020; Canadell et al., 2021], Canada accounts for an estimated 1.1% of the global total (corresponding to ~0.07% of total enhanced anthropogenic radiative forcing). In comparison, Canada consumed on average 2.7 Tg N/yr of synthetic N fertilizer over 2016–2020, representing 2.4% of total world consumption of 110 Tg N/yr [Food and Agriculture Organization of the U. N. FAO, 2022]. Assuming that synthetic N fertilizer is the main driver of the anthropogenic $N_2O$ source, Canada's emissions appear commensurate with, if not substantially lower than, its share of fertilizer consumption.

The $N_2O$ seasonal cycle in Canadian Cropland has a dual maximum structure similar to that seen in the U.S. Midwest, with seasonal peaks in March and June [Nevison et al., 2018]. The June peak is associated with the agricultural growing season, while the March peak is likely a freeze-thaw signal associated with a burst of microbial activity in previously frozen but recently thawed soil [Wagner-Riddle et al., 2017; Del Grosso et al., 2022; Nevison et al., 2023]. Unlike some estimates in the literature and by global inventories [Wagner-Riddle et al., 2017; EDGAR, 2017; Janssens-Maenhout et al., 2019], the summer peak in Canadian Cropland is comparable to, or in some configurations greater than, the late winter/early spring peak.

### 4.4. Impact of environment Canada data on the inversion

The inclusion of ECCC data in CT-L tends to preferentially enhance the June peak in the posterior $N_2O$ flux relative to the March peak. The fact that ECCC data tend to weaken the March pulse suggests that the presumed freeze-thaw signal in March is driven in part from U.S. Midwest $N_2O$ data that have 10-day back trajectory footprints in Canada. However, the late winter peak in the U.S. Midwest is centered around mid-March, about 10 days earlier than the Canadian Crop winter peak, which suggests that data north of the Midwest Corn/Soybean belt also contribute to the seasonal patterns and help drive the early peak later toward the end of March [Nevison et al., 2023].

Of the four ECCC sites considered here, EGB has the largest impact on the inversion and is the main reason for the modest 10–25% increase in the total flux from Canadian Cropland relative to the NOAA only configuration (Table 2). EGB has the greatest impact in part because it is the most heavily sampled site, with twice as many days of *in situ* data than the other ECCC sites (Table 1). Notably, EGB is located near Toronto, and thus may be influenced by $N_2O$ sources from industry and fossil fuel combustion. Indeed the *in situ* $N_2O$ time series at EGB is characterized by variability suggestive more of urban pollution and noise than of discernible agricultural signals.

EGB sits at 44°N, which is the same latitude as South Dakota and southern Minnesota in the U.S. corn/soybean belt. This is far south of most western Canadian cropland, which accounts for 80% or more of total Canadian Cropland $N_2O$ emissions in all CT-L configurations. While strong March $N_2O$ peaks are evident in CT-L results from the U.S. corn/soybean belt at 44°N, CT-L predicts no March peak and only a small June peak in cropland integrated over southern Ontario and Quebec (i.e., Canadian Cropland restricted to regions east of 95°W). This result supports the hypothesis above that the agricultural signals in Canadian Cropland are driven in part from U.S. Midwest $N_2O$ data with 10-day back trajectory footprints that originate in western Canada but generally don't extend into eastern Canada.

The main reason for the modest impact of ECCC data on Canadian emissions is that there are few strong excursions from background at any Canadian sites, including the NOAA LLB site and the ECCC ETL site. Since the inversion is based on the difference between observed $N_2O$ and the prescribed background value, the increased coverage does not have a major impact on the overall fluxes. It does, however, modestly improve the confidence in the inversion results, through ~5–15% increases in the posterior flux uncertainty reduction. In general, these results suggest that even the addition of many new $N_2O$ monitoring sites will not lead to a major increase in the estimated flux from Canada, unless a site situated in the heart of Canadian Cropland detects strong excursions from background on par with those observed at the NOAA site in Iowa [Nevison et al., 2018, 2023]. Two existing sites in the ECCC methane and $CO_2$ monitoring network, Bratt's Lake, Saskatchewan (50.2°N, −104.7°W), located on a working grain farm, and Esther, Alberta (51.7°N, −110.2°W), located in cattle ranchland, appear best situated to capture potentially strong agricultural fluxes, but to date $N_2O$ has not been monitored at these sites [Global Atmosphere Watch, 2023]. Meawhile, only modest excursions in $N_2O$ from background levels are observed at the NOAA aircraft site in North Dakota, which is located just southwest of the main Canadian agricultural belt. On a related note, despite field reports of significant $N_2O$ emissions from tundra and permafrost [Repo et al., 2009; Voigt et al., 2020], these emissions do not have a discernible impact as yet on long-term Canadian monitoring sites.

## 5. Conclusions

Inclusion of 4 new Environment and Climate Change Canada (ECCC) sites in the CarbonTracker-Lagrange (CT-L) regional inversion leads to small net increases in Canadian $N_2O$ emissions and modest improvements in posterior flux uncertainty by 10 ± 5% over central Canada. However, the absolute uncertainty reduction relative to the prior is at best 35%. The relatively small impact of the ECCC sites on CT-L results is due largely to the fact that $N_2O$ is generally close to background at those sites, with no strong excursions from background. CT-L results in Canada are relatively consistent across two different particle dispersion models.

CT-L predicts a total $N_2O$ flux of ~0.08 ± 0.08 Tg N/yr from Canadian Cropland, although this total may also include urban influences from the Toronto metropolitan area. The Canadian Cropland flux has a dual maxima pattern, similar to that found in the U.S. Midwest, but in which the March (presumed freeze-thaw related) peak is more comparable in magnitude to the June growing season peak. Emissions from Canada as a whole are not well resolved by either CT-L or global inversions, due in part to the sparsity of Canadian monitoring sites, but probably more importantly due to the lack of a strong signal in atmospheric $N_2O$ data at existing Canadian sites.

## Funding statement

CDN acknowledges support from NASA award 80NSSC20K1804.

## Author contribution statement

CDN performed the inversions, analyzed the results and wrote the manuscript. XL provided the NOAA atmospheric $N_2O$ data used in the inversion. DW provided the ECCC atmospheric $N_2O$ data used in the inversion. HT supplied the global inversion results used to compare to the regional inversion. All authors read and approved the manuscript.

## Declaration of competing interest

The authors declare that they have no known competing financial interests or personal relationships that could have appeared to influence the work reported in this paper.

## Data availability

Data will be made available on request.

## Acknowledgments

The authors are grateful to Arlyn Andrews, Kirk Thoning and Lei Hu for developing and providing guidance on the inversion framework. We thank Thomas Nehrkorn, Marikate Mountain and Mike Trudeau for providing model influence footprints and Ed Dlugokencky, Robert Kessler and the many people who have contributed to the production of

the excellent $N_2O$ datasets that have made this study possible.

## Appendix A. Supplementary data

Supplementary data to this article can be found online at https://doi.org/10.1016/j.atmosenv.2023.120075.

## References


Andrews, A.E., Kofler, J.D., Trudeau, M.E., Williams, J.C., Neff, D.H., et al., 2014. $CO_2$, CO, and $CH_4$ measurements from tall towers in the NOAA Earth System Research Laboratory's Global Greenhouse Gas Reference Network: instrumentation, uncertainty analysis, and recommendations for future high-accuracy greenhouse gas monitoring efforts. Atmos. Meas. Tech. 7, 647–687. https://doi.org/10.5194/amt-7-647-2014. www.atmos-meas-tech.net/7/647/2014/.

Andrews, A., Crotwell, A., Crotwell, M., Handley, P., Higgs, J., Kofler, J., Lan, X., Legard, T., Madronich, M., McKain, K., Miller, J., Moglia, E., Mund, J., Neff, D., Newberger, T., Petron, G., Turnbull, J., Vimont, I., Wolter, S., NOAA Global Monitoring Laboratory, 2022. NOAA global greenhouse gas reference network flask-air PFP sample measurements of N2O at tall tower and other continental sites, 2005-present. https://doi.org/10.15138/C11N-KD82. Version: 2022-11-01.

Beaulieu, J., Tank, J., Hamilton, S., Wollheim, W., Hall, R., Mulholland, P., Peterson, B., Ashkenas, L., Cooper, L., Dahm, C., et al., 2011. Nitrous oxide emission from denitrification in stream and river networks. Proc. Natl. Acad. Sci. USA 108, 214–219.

Canadell, J.G., Monteiro, P.M.S., Costa, M.H., Cotrim da Cunha, L., Cox, P.M., Eliseev, A. V., Henson, S., Ishii, M., Jaccard, S., Koven, C., Lohila, A., Patra, P.K., Piao, S., Rogelj, J., Syampungani, S., Zaehle, S., Zickfeld, K., 2021. Global carbon and other biogeochemical cycles and feedbacks. In: Masson-Delmotte, V., Zhai, P., Pirani, A., Connors, S.L., Péan, C., Berger, S., Caud, N., Chen, Y., Goldfarb, L., Gomis, M.I., Huang, M., Leitzell, K., Lonnoy, E., Matthews, J.B.R., Maycock, T.K., Waterfield, T., Yelekçi, O., Yu, R., Zhou, B. (Eds.), Climate Change 2021: the Physical Science Basis. Contribution of Working Group I to the Sixth Assessment Report of the Intergovernmental Panel on Climate Change. Cambridge University Press, Cambridge, United Kingdom and New York, NY, USA, pp. 673–816. https://doi.org/10.1017/9781009157896.007.

Ciais, P., Sabine, C., Bala, G., Bopp, L., Brovkin, V., Canadell, J., Chhabra, A., DeFries, R., Galloway, J., Heimann, M., Jones, C., Le Qur, C., Myneni, R.B., Piao, S., Thornton, P., 2013. Carbon and other biogeochemical cycles. In: Stocker, T.F., Qin, D., Plattner, G.-K., Tignor, M., Allen, S.K., Boschung, J., Nauels, A., Xia, Y., Bex, V., Midgley, P.M. (Eds.), Climate Change 2013: the Physical Science Basis. Contribution of Working Group I to the Fifth Assessment Report of the Intergovernmental Panel on Climate Change. Cambridge University Press, Cambridge, United Kingdom and New York, NY, USA.

Crutzen, P.J., Mosier, A.R., Smith, K.A., Winiwarter, W., 2008. $N_2O$ release from agro-biofuel production negates global warming reduction by replacing fossil fuels. Atmos. Chem. Phys. 8, 389–395.

Deng, Z., Ciais, P., Tzompa-Sosa, Z., Saunois, M., Qiu, C., Tan, C., Su, T., Ke, P., Cui, Y., Tanaka, K., et al., 2022. Comparing national greenhouse gas budgets reported in UNFCCC inventories against atmospheric inversions. Earth Syst. Sci. Data 14, 1639–1675.

Draxler, R.R., Hess, G.D., 1998. An overview of the HYSPLIT_4 modeling system of trajectories, dispersion, and deposition. Aust. Meteorol. Mag. 47, 295–308.

EDGAR, 2009. European commission, joint research centre (JRC)/Netherlands environmental assessment agency (PBL): emission database for global atmospheric research (EDGAR). release version 4.0. http://edgar.jrc.ec.europa.eu.

EDGAR4.3.2., 2017. Emissions database for global atmospheric research. *version 4.3.2* European Commission. Retrieved from. https://edgar.jrc.ec.europa.eu/overview.php?v%3D432_GHG. https://data.europa.eu/doi/10.2904/JRC-DATASET-EDGAR.

Food and Agriculture Organization of the U. N. (FAO), 2022. Production and Trade Statistics. Food and Agric. Org. of the U. N., Rome. Available at. http://faostat.fao.org/.

Gamble, R., Heaney, D., 2022. The economics of 4R BMP implementation and emissions reductions from fertilizer: an industry perspective on financial implications of the 30% nitrous oxide emission reduction target. https://fertilizercanada.ca/wp-content/uploads/2022/09/Economics-of-4R-BMP-Implementation-and-Emissions-Reductions-from-Fertilizer.pdf.

Global atmosphere watch station information system (GAWSiS). https://gawsis.meteoswiss.ch/GAWSIS//index.html#/, 2023–. (Accessed 26 May 2023).

Hall, B.D., Dutton, G.S., Elkins, J.W., 2007. The NOAA nitrous oxide standard scale for atmospheric observations. J. Geophys. Res. 112, D09305 https://doi.org/10.1029/2006JD007954.

Janssens-Maenhout, G., Crippa, M., Guizzardi, D., Muntean, M., Schaaf, E., Dentener, F., et al., 2019. EDGAR v4.3.2 Global Atlas of the three major greenhouse gas emissions for the period 1970–2012. Earth Syst. Sci. Data 11 (3), 959–1002. https://doi.org/10.5194/essd-11-959-2019.

Lan, X., Dlugokencky, E.J., Mund, J.W., Crotwell, A.M., Crotwell, M.J., Moglia, E., Madronich, M., Neff, D., Thoning, K.W., 2022a. Atmospheric Nitrous Oxide Dry Air Mole Fractions from the NOAA GML Carbon Cycle Cooperative Global Air Sampling Network 1997–2021. https://doi.org/10.15138/53g1-x417. Version: 2022-11-21.

Lan, X., Thoning, K.W., Dlugokencky, E.J., 2022b. Trends in globally-averaged $CH_4$, $N_2O$, and $SF_6$ determined from NOAA global monitoring laboratory measurements. *Version 2022-11*. https://doi.org/10.15138/P8XG-AA10.

Lin, J.C., Gerbig, C., Wofsy, S.C., Andrews, A.E., Daube, B.C., Davis, K.J., Grainger, C.A., 2003. A near-field tool for simulating the upstream influence of atmospheric observations: the Stochastic Time-Inverted Lagrangian Transport (STILT) model. J. Geophys. Res. 108 (D16), 4493. https://doi.org/10.1029/2002JD003161.

MacFarling Meure, C., Etheridge, D.M., Trudinger, C.M., Steele, L.P., Langenfelds, R.L., van Ommen, T., Smith, A., Elkins, J.W., 2006. Law Dome $CO_2$, $CH_4$, and $N_2O$ ice core records extended to 2000 years BP. Geophys. Res. Lett. 33, L14810 https://doi.org/10.1029/2006GL026152.

McKain, K., Sweeney, C., Baier, B., Crotwell, A., Crotwell, M., Handley, P., Higgs, J., Legard, T., Madronich, M., Miller, J.B., Moglia, E., Mund, J., Neff, D., Newberger, T., Wolter, S., NOAA Global Monitoring Laboratory, 2022. NOAA global greenhouse gas reference network flask-air PFP sample measurements of $CO_2$, $CH_4$, CO, $N_2O$, $H_2$, $SF_6$ and isotopic ratios collected from aircraft vertical profiles *[Data set]. Version: 2022-12-01*. https://doi.org/10.15138/39HR-9N34.

Miller, S.M., et al., 2012. Regional sources of nitrous oxide over the United States: seasonal variation and spatial distribution. J. Geophys. Res. Atmos. 117, D06310.

National oceanic atmospheric administration (NOAA) global monitoring division, interactive data visualization. https://www.esrl.noaa.gov/gmd/dv/iadv/. (Accessed 20 September 2022).

Nehrkorn, T., Eluszkiewicz, J., Wofsy, S., Lin, J., Gerbig, C., Longo, M., Freitas, S., 2010. Coupled weather research and forecasting–stochastic time-inverted Lagrangian transport (WRF–STILT) model. Meteorol. Atmos. Phys. 107 (1–2), 51–64. https://doi.org/10.1007/s00703-010-0068-x.

Nevison, C., Andrews, A., Thoning, K., Dlugokencky, E., Sweeney, C., Miller, S., et al., 2018. Nitrous oxide emissions estimated with the CarbonTracker-Lagrange North American regional inversion framework. Global Biogeochem. Cycles 32. https://doi.org/10.1002/2017GB005759.

Nevison, C., Lan, X., Ogle, S.M., 2023. Remote sensing soil freeze-thaw status and North American $N_2O$ emissions from a regional inversion. Global Biogeochem. Cycles 37, e2023GB007759. https://doi.org/10.1029/2023GB007759.

Park, S., et al., 2012. Trends and seasonal cycles in the isotopic composition of nitrous oxide since 1940. Nat. Geosci. 5, 261–265.

Patra, P.K., Takigawa, M., Watanabe, S., Chandra, N., Ishijima, K., Yamashita, Y., 2018. Improved chemical tracer simulation by MIROC4. 0-based atmospheric chemistry-transport model (MIROC4-ACTM). Inside Solaris 14, 91–96.

Prather, M.J., Froidevaux, L., Livesey, N.J., 2023. Observed changes in stratospheric circulation: decreasing lifetime of $N_2O$, 2005–2021. Atmos. Chem. Phys. 23, 843–849. https://doi.org/10.5194/acp-23-843-2023.

Ravishankara, A., Daniel, J., Portmann, R., 2009. The dominant ozone-depleting substance emitted in the 21st century. Science 326, 123–125.

Repo, M.E., Susiluoto, S., Lind, S.E., Jokinen, S., Elsakov, V., Biasi, C., et al., 2009. Large N2O emissions from cryoturbated peat soil in tundra. Nat. Geosci. 2 (3), 189–192.

Saikawa, E., et al., 2014. Global and regional emissions estimates for $N_2O$. Atmos. Chem. Phys. 14, 4617–4641.

Schlesinger, W.H., 2013. An estimate of the global sink for nitrous oxide in soils. Global Change Biol. 19, 2929–2931. https://doi.org/10.1111/gcb.2239.

Stein, A.F., Draxler, R.R., Rolph, G.D., Stunder, B.J.B., Cohen, M.D., Ngan, F., 2015. NOAA's HYSPLIT atmospheric transport and dispersion modeling system. Bull. Am. Meteorol. Soc. 96, 2059–2077. https://doi.org/10.1175/BAMS-D-14-00110.1.

Stocker, B.D., Roth, R., Joos, F., Spahni, R., Steinacher, M., Zaehle, S., et al., 2013. Multiple greenhouse- gas feedbacks from the land biosphere under future climate change scenarios. Nat. Clim. Change 3 (7), 666–672.

Sweeney, C., Karion, A., Wolter, S., Newberger, T., Guenther, D., et al., 2015. Seasonal climatology of $CO_2$ across North America from aircraft measurements in the NOAA/ESRL global greenhouse gas reference network. J. Geophys. Res. Atmos. 120, 5155–5190. https://doi.org/10.1002/2014JD022591.

Thompson, R.L., et al., 2014. TransCom $N_2O$ model inter-comparison Part 2: atmospheric inversion estimates of $N_2O$ emissions. Atmos. Chem. Phys. 14, 6177–6194. https://doi.org/10.5194/acp-14-6177-2014.

Tian, H., Xu, R., Canadell, J.G., et al., 2020. A comprehensive quantification of global nitrous oxide sources and sinks. Nature 586, 248–256. https://doi.org/10.1038/s41586-020-2780-0.

Voigt, C., Marushchak, M.E., Abbott, B.W., Biasi, C., Elberling, B., Siciliano, S.D., et al., 2020. Nitrous oxide emissions from permafrost-affected soils. Nat. Rev. Earth Environ. 1 (8), 420–434.

Wagner-Riddle, C., Congreves, K.A., Abalos, D., Berg, A.A., Brown, S.E., Ambadan, J.T., Gao, X., Tenuta, M., 2017. Globally important nitrous oxide emissions from croplands induced by freeze–thaw cycles. Nat. Geosci. https://doi.org/10.1038/NGEO2907.

Wells, K.C., Millet, D.B., Bousserez, N., Henze, D.K., Chaliyakunnel, S., Griffis, T.J., et al., 2015. Simulation of atmospheric $N_2O$ with GEOS-Chem and its adjoint: evaluation of observational constraints. Geosci. Model Dev. (GMD) 8 (10), 3179–3198. https://doi.org/10.5194/gmd-8-3179-2015.

Wells, K.C., Millet, D.B., Bousserez, N., Henze, D.K., Griffis, T.J., Chaliyakunnel, S., Dlugokencky, E.J., Saikawa, E., Xiang, G., Prinn, R.G., et al., 2017. Top-down constraints on global $N_2O$ emissions at optimal resolution: application of a new dimension reduction technique. Atmos. Chem. Phys. 18, 735–756. https://doi.org/10.5194/acp-18-735-2018.

Wilson, C., Chipperfield, M.P., Gloor, M., Chevallier, F., 2014. Development of a variational flux inversion system (INVICAT v1. 0) using the TOMCAT chemical transport model. Geosci. Model Dev. (GMD) 7, 2485–2500.

Xu, R., Tian, H., Pan, N., Thompson, R.L., Canadell, J.G., Davidson, E.A., et al., 2021. Magnitude and uncertainty of nitrous oxide emissions from North America based on bottom-up and top-down approaches: informing future research and national inventories. Geophys. Res. Lett. 48, e2021GL095264 https://doi.org/10.1029/2021GL095264.

Yadav, V., Michalak, A.M., 2013. Improving computational efficiency in large linear inverse problems. Geosci. Model Dev. (GMD) 6 (3), 583–590.